FtsZ treadmilling is essential for Z-ring condensation and septal constriction initiation in bacterial cell division

Kevin D. Whitley[1,2+], Calum Jukes[1+], Nicholas Tregidgo[1], Eleni Karinou[1], Pedro Almada[3], Ricardo Henriques[3], Cees Dekker[2], and Séamus Holden[1*]

[1]Centre for Bacterial Cell Biology, Biosciences Institute, Faculty of Medical Sciences, Newcastle University, Newcastle upon Tyne, UK; [2]Department of Bionanoscience, Kavli Institute of Nanoscience Delft, Delft University of Technology, Delft, The Netherlands; [3]MRC-Laboratory for Molecular Cell Biology, University College London, London, UK

*Corresponding author: seamus.holden@ncl.ac.uk

+Equal author contribution

ABSTRACT

Despite the central role of division in bacterial physiology, how division proteins work together as a nanoscale machine to divide the cell remains poorly understood. Cell division by cell wall synthesis proteins is guided by the cytoskeleton protein FtsZ, which assembles at mid-cell as a dense Z-ring formed of motile treadmilling filaments[1,2]. However, although FtsZ treadmilling is essential for cell division, the function of FtsZ treadmilling motility remains unclear[2–5]. Here, we systematically resolve the function of FtsZ treadmilling across each stage of division in the Gram-positive model organism *Bacillus subtilis* using a novel combination of nanofabrication, advanced microscopy, and microfluidics to measure the division-protein dynamics in live cells with ultrahigh sensitivity. We find that FtsZ treadmilling has two essential functions: mediating condensation of diffuse FtsZ filaments into a dense Z-ring, and initiating constriction by guiding septal cell wall synthesis. After constriction initiation, FtsZ treadmilling has a dispensable function in accelerating septal constriction rate. Our results show that FtsZ treadmilling is critical for assembling and initiating the bacterial cell division machine.

INTRODUCTION

Bacterial cell division is an essential cellular process and a key target for antibiotics. Bacterial cell division is also a remarkable feat of molecular self-assembly where a nanoscale divisome machine builds a micron-scale wall (septum) at mid-cell. The core components of this machine include the septal cell-wall synthases that insert new peptidoglycan (PG) to build the septum, and the essential cytoskeletal tubulin homologue FtsZ that polymerises into a dense "Z-ring" band of short filaments at mid-cell[6–8]. These short FtsZ filaments move by treadmilling, a type of motion where an asymmetric filament undergoes plus-end polymerisation and minus-end depolymerisation, with GTP hydrolysis setting the rate of FtsZ depolymerisation and overall treadmilling speed[1,2,9]. FtsZ treadmilling dynamics are essential for cell division[2–5].

However, the role of FtsZ treadmilling in cell division remains unclear. In the Gram-positive model organism *Bacillus subtilis*, we previously observed that constriction rate and synthase speed was dependent upon FtsZ filament speed[1], leading to an initial model of a tightly coupled motile cytoskeleton-synthase complex, where FtsZ acts an obligatory guide and rate-limiting step for septal PG synthesis. In contrast, FtsZ treadmilling is dispensable after constriction initiation in *Staphylococcus aureus*[3], even though the two organisms belong to the same phylogenetic class. This could reflect genuine differences between species, or there may exist a common division mechanism where FtsZ treadmilling plays different roles at different cell cycle stages. To date, it remains unclear how the role of treadmilling FtsZ filaments varies across the full cell cycle.

Here, we measure the dynamics and function of FtsZ treadmilling across the cell cycle in *B. subtilis*. To make these observations, we developed a new method combining nanofabrication, advanced microscopy, and microfluidics. This approach allowed us to measure native FtsZ dynamics at near-single-filament resolution throughout the cell cycle. We found that treadmilling dynamics drive FtsZ filament interactions during Z-ring assembly and that the FtsZ motility stabilises filaments into dense Z-rings. We determined that the FtsZ inhibitor PC190723 arrests FtsZ treadmilling within seconds, independent of cell cycle stage, allowing us to elucidate the rapid response of cells to treadmilling arrest. By systematically determining the response of single cells to FtsZ treadmilling arrest by PC190723, we found that FtsZ treadmilling has two separate essential functions: mediating Z-ring assembly during the earliest stage of cell division, and subsequently for guiding septal constriction initiation. We found that FtsZ treadmilling becomes dispensable after constriction initiation but increases septal constriction rate. Our results show that the key roles of FtsZ treadmilling are to drive Z-ring assembly and to initiate septal constriction.

RESULTS

FtsZ assembly at mid-cell has three distinct phases: nascent, mature, and constricting Z-rings

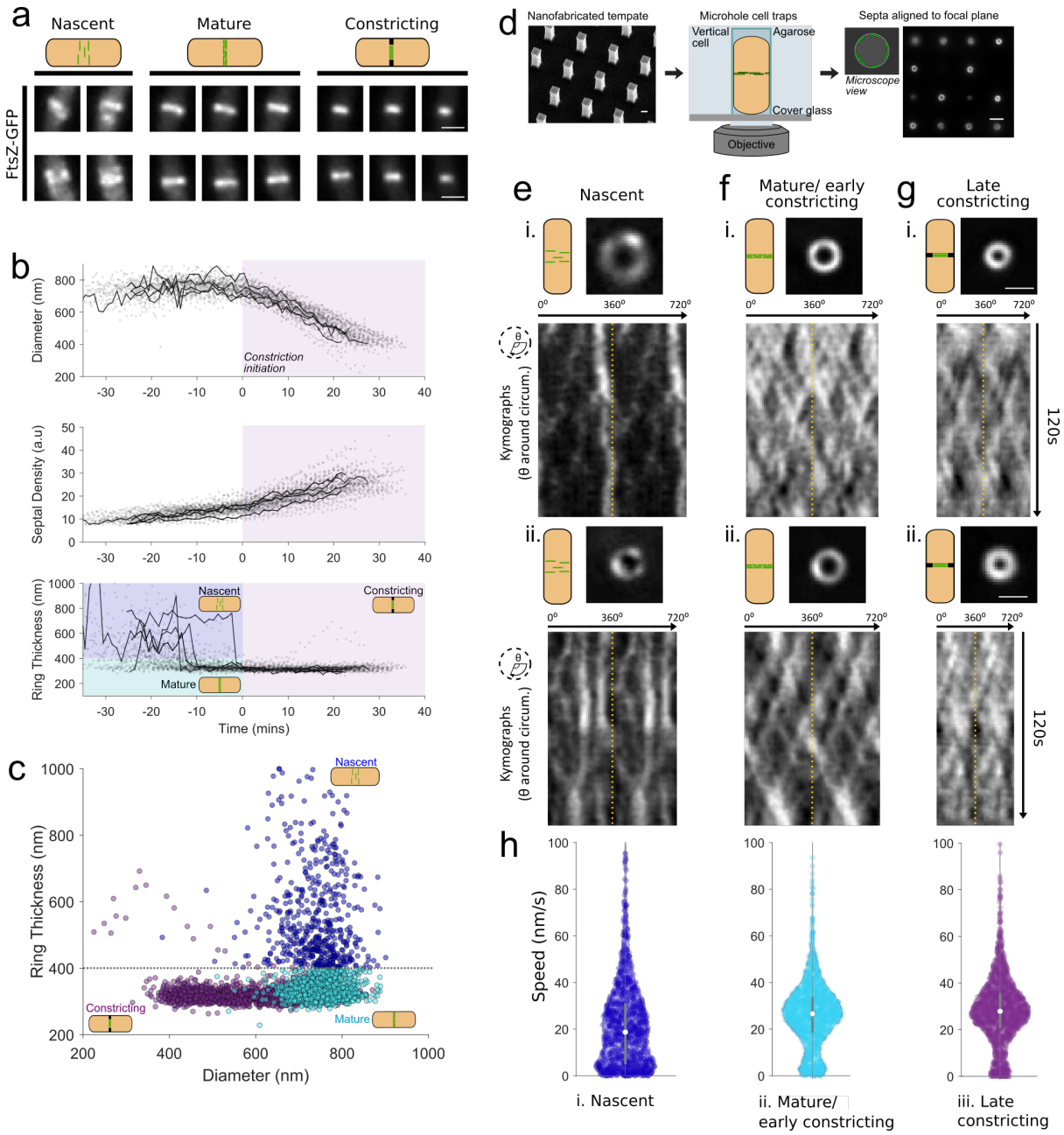

Figure 1. FtsZ filament organisation and dynamics throughout the division cycle. *(a) Exemplar images of FtsZ-GFP (SH130) filament organisation over the division cycle, classified by division phase. (b) Quantification of FtsZ-ring diameter, ring thickness and septal density (septal intensity divided by ring circumference) over cell cycle from time-lapse microscopy data*. Nascent Z-rings have large axial width (ring thickness) due to the diffuse distribution of filaments, which condense into a thin mature Z-ring, followed by constriction initiation. Traces are temporally aligned relative to the start time of constriction (Methods). Grey scatter points represent all data points, black lines show individual, representative traces. *(c) Classification of Z-ring stage via ring thickness and relative septal diameter.* Nascent Z-rings (blue) have a ring thickness greater than 400 nm (dashed line) and unconstricted septum. Mature rings (cyan) have a ring thickness less than 400 nm and unconstricted septum. Constricting rings (purple) have a constricted septum. *(d) VerCINI schematic.* Rod-shaped bacteria are trapped in agarose microholes, rotating the division septum into microscope imaging plane. *(e-g) VerCINI microscopy of FtsZ filament dynamics for each Z-ring phase, two representative examples per phase (i-ii)*. Nascent Z-rings are composed of sparse filaments diffusely distributed around the circumference of the cell, and a large fraction of static FtsZ filaments. Mature and constricting Z-rings possess a more uniform distribution of FtsZ filaments around the division site, with most filaments treadmilling. Images of septa show the first frame in kymographs (t=0 s). Kymographs were obtained by fitting septal images to circles and plotting intensity values around the circumference of the cell for each frame of the time-lapse (1 frame/ s).

Two full revolutions around the cell (0-720°) are plotted side-by-side in each kymograph to resolve filament trajectories that pass 0°/360°, separated by yellow dotted lines. *(h) Violin plots of FtsZ filament speed for each Z-ring phase.* White circles, median; grey lines, interquartile range.

We first determined FtsZ organisation during cell division in *B. subtilis* using an FtsZ-GFP fusion[10] expressed from the native locus at wild-type protein levels (SH130, Methods, Supplementary Figure 1). Cell morphology analysis showed near native morphology at 30°C and only a mild elongation phenotype at 37°C (Supplementary Figure 2).

We performed time-lapse imaging of FtsZ-GFP organisation in slow growth conditions (Figure 1; Supplementary Video 1). We observed that FtsZ filaments initially formed a diffuse structure at mid-cell which rapidly condensed into a dense narrow band, followed by the onset of constriction (Figure 1a). We quantified these changes in Z-ring structure by measuring the dimensions (thicknesses and diameters) and septal density (total septal intensity divided by Z-ring circumference) of the Z-rings in each frame (Methods). The resulting traces of thicknesses and diameters over time were aligned by the start time of constriction (Methods, Figure 1b). These time traces revealed three distinct Z-ring stages that we classified as 'nascent', 'mature', and 'constricting' (Figure 1b, Supplementary Note 3). During the nascent Z-ring stage, low density FtsZ filaments transiently assemble at mid-cell over a wide region, consistent with previous reports[4,13–15]. FtsZ filaments then rapidly condense into a thin mature Z-ring structure, which remains unconstricted but increases in intensity for some time. Finally, the Z-ring begins constricting until division is finished.

VerCINI microscopy reveals FtsZ filament dynamics are cell cycle regulated and FtsZ treadmilling drives filament encounter in nascent Z-rings

FtsZ filament dynamics are difficult to observe *in vivo*. TIRF imaging only illuminates a thin slice of the septum, limiting observation to partial snapshots of filament dynamics in nascent Z-rings[1,2]. We previously developed a prototype approach which resolves this problem by vertically immobilizing cells in nanofabricated chambers, allowing continuous imaging of the entire division septum, including dense actively constricting Z-rings[1,4]. However, the prototype method was not capable of imaging dim, nascent Z-rings due to high background, suffered from fast photobleaching and lacked the throughput required for cell cycle studies.

Hence, we created an entirely redesigned vertical cell immobilisation method which addresses all of these issues and allows ultrasensitive high-resolution imaging of FtsZ filament dynamics at all stages of the cell cycle, termed VerCINI (Vertical Cell Imaging by Nanostructured Immobilisation). This new method features a high-throughput chip design, centrifugation loading, high SNR ring-HiLO illumination[16], imaging denoising[17], and custom septal localisation and background subtraction algorithms (Methods, Supplementary Figure 3-4, Supplementary Videos 2-3). We measured FtsZ filament dynamics during each division stage using VerCINI (Figure 1, Supplementary Figure 5, Supplementary Videos 4-6)[1,21]. Division stage was determined based on septal intensity and diameter (Methods, Supplementary Figure 6, Supplementary Note 3).

In nascent Z-rings, we observed that FtsZ filaments are sparsely distributed, with a mixture of motile and static filaments (Figure 1f, Supplementary Figure 7a, 35% immobile, filament speed < 10 nm/s), leading to a low average filament speed with large spread (median 19 nm/s, interquartile range, IQR, 5-31, N=526). Surprisingly, we frequently observed two or more motile FtsZ filaments colliding, leading to aggregation and temporary motion arrest of both filaments (Figure 1eii, Supplementary Figure 5). FtsZ filament aggregation by lateral filament interactions is required to bundle FtsZ filaments and condense the Z-ring[22–26]. These data show that FtsZ treadmilling motility can drive filament aggregation by promoting the filament encounters required for lateral interactions.

Z-ring condensation led to a drop in the number of immobile FtsZ filaments in mature/early constricting Z-rings, yielding a significant increase in average filament speed with narrower speed distribution (15% immobile, median 27 nm/s, IQR 19-34, N=1053). Filament speeds in late constricting Z-rings were similar to those of mature/early constricting Z-rings (13% immobile, median speed 28 nm/s, IQR 21-36, N=1677). Due to the decreased immobile population, filaments in mature and constricting Z-rings traversed, on average, twice the distance around the septum of those in nascent rings (Supplementary Figure 7c). The FtsZ filament lifetime (time bound to the septum) was similar at each stage of cell division: that is, although FtsZ filaments in the nascent stage are less dense and less motile, their bound lifetime remains similar (Supplementary Figure 7b). The results show that FtsZ treadmilling dynamics are cell-cycle regulated, with FtsZ treadmilling promoting Z-ring condensation prior to septal constriction initiation.

PC190723 arrests FtsZ treadmilling within seconds throughout division

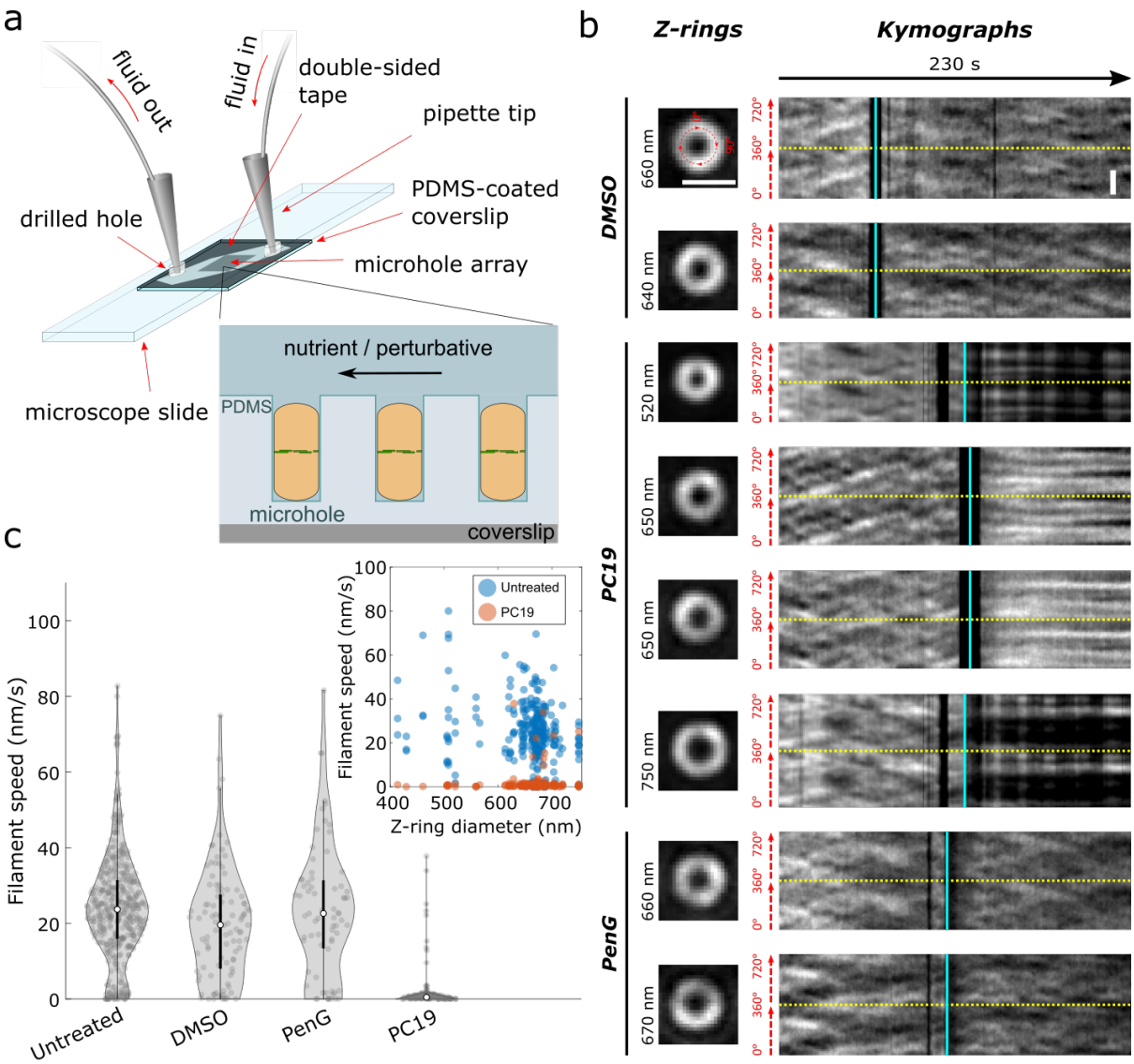

Figure 2. PC190723 arrests cellular FtsZ treadmilling within seconds across all stages of constriction. *(a) Schematic of microfluidic VerCINI.* Rod-shaped cells are confined in open-topped microholes in a thin layer of PDMS atop a microscope coverslip as solutions flow over them. The flow channel is formed from a cut piece of double-sided tape sandwiched between the PDMS layer and a microscope cover slide with drilled holes to allow inlet and outlet tubes. *(b) Representative images of septa and associated kymographs of FtsZ-GFP (SH130) dynamics in vertically-immobilised cells during rapid treatment with either DMSO (top), PC19 (middle), or PenG (bottom) at multiple septal diameters.* Images of septa show the first frame in kymographs (t=0 s). Kymographs were obtained by fitting septal images to circles and plotting intensity values around the

circumference of the cell for each frame of the time-lapse (1 frame/s). Two full revolutions around the cell (0-720°) are plotted side-by-side in each kymograph to resolve filament trajectories that pass 0°/360°, separated by yellow dotted lines. Cyan lines show arrival time of media containing DMSO, PenG, or PC19. Black bands around time of treatment resulted from a loss of focus during fluid exchange. Fluctuations in intensity for two septa post-PC19 treatment (750 nm and 520 nm diameter septa) resulted from manual refocusing during imaging. Scale bars: 1000 nm. *(c) Violin plots of FtsZ treadmilling speeds pre- and post-treatment measured from kymographs.* White circles, median; thick grey lines, interquartile range. *Inset:* FtsZ treadmilling speed distributions for untreated (white circles) and PC19-treated (red circles) cells from violin plots separated by septal diameter.

We next set out to determine the function of FtsZ treadmilling during each stage of cell division. For this we needed to observe the effect on cell division in response to rapid FtsZ treadmilling arrest. The antibiotic PC190723 (PC19) arrests FtsZ treadmilling by specifically inhibiting FtsZ GTP hydrolysis[1,18]. Since the entire cell division process takes only 10-20 minutes in fast growth conditions, it was critical to determine whether PC19 acted sufficiently rapidly and robustly for use in dissecting the effect of treadmilling during each cell cycle stage. To determine how PC19 and other cell division inhibitors perturb FtsZ treadmilling, we developed microfluidic VerCINI, which combines high-resolution imaging of cell division protein dynamics *in vivo* with rapid chemical perturbation (Methods, Figure 2a). In this method, cells are confined in an array of open-topped microholes formed from PDMS atop a microscope coverslip, which is contained within a microfluidic chamber. A real-time image-based autofocus system was used to stabilise focus during high-speed imaging[19].

We imaged FtsZ-GFP (SH130) using microfluidic VerCINI to observe the effects of division inhibitors PC19 and Penicillin G (PenG) on FtsZ treadmilling. We recorded untreated FtsZ dynamics for 90 s while blank media flowed over the cells, then continuously treated cells with an excess of division inhibitor by changing fluid flow to media laced with the compound (Figure 2b, Supplementary Video 7). FtsZ treadmilling dynamics were abolished by PC19 within a few seconds for all diameters of septa observed (Figure 2c). When we treated cells with Penicillin G (PenG), which inhibits cell wall synthesis by binding to cell wall synthase transpeptidation sites, FtsZ dynamics continued unperturbed for the duration of the experiment (several minutes). FtsZ dynamics were also unaffected by a DMSO-only control, the solvent for PC19 (Figure 2c, Supplementary Videos 8-9).

By providing high spatiotemporal resolution during rapid chemical perturbation, microfluidic VerCINI revealed the effect of division inhibitors on FtsZ treadmilling throughout division. Our results demonstrate that PC19 inhibits FtsZ treadmilling within seconds well after the start of constriction, whereas PenG treatment does not directly affect FtsZ dynamics.

175 **FtsZ treadmilling is essential for Z-ring condensation and septal constriction initiation, but is**
176 **subsequently dispensable**

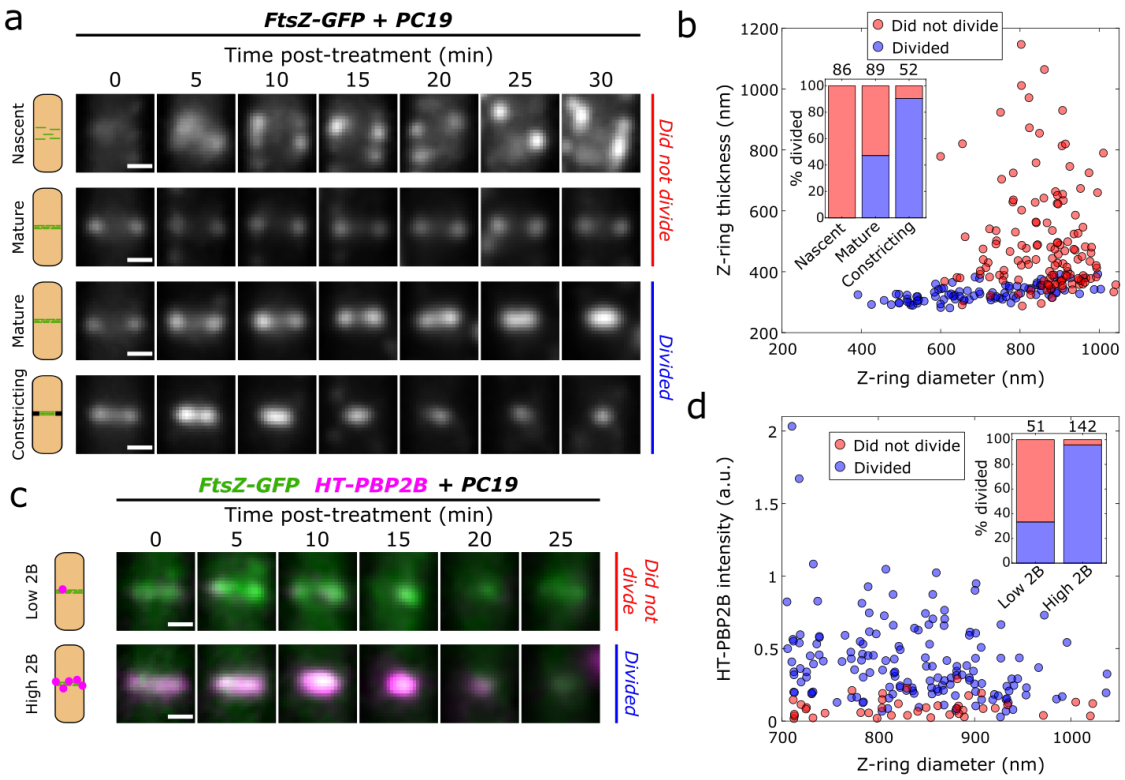

177

178 **Figure 3. FtsZ treadmilling is required until the arrival of PG synthesis machinery.** *(a) Representative time-lapses of Z-rings*
179 *for FtsZ-GFP cells (SH130) after arrival of 10 µM PC19-laced media.* Nascent rings and many mature rings do not divide for
180 tens of minutes after PC19 treatment, whereas constricting rings and many mature rings continue dividing after treatment.
181 *(b) Scatter plot of Z-ring diameters and thicknesses for all FtsZ-GFP cells at t=0 min showing whether they continued dividing*
182 *(blue) or not (red). Inset*: Percentage of cells that continued dividing classified by division stage. Nascent: thickness>400 nm,
183 mature: thickness>400 nm, diameter>700 nm, constricting: thickness<400 nm, diameter<700 nm. *(c) Representative time-*
184 *lapses of rings from two-colour strain SH212 (Green: FtsZ-GFP, magenta: HaloTag-PBP2B) after the arrival of PC19-laced*
185 *media.* Z-rings with low HT-PBP2B signal typically do not continue dividing while those with high signal typically do. *(d) Scatter*
186 *plot of Z-ring diameters and normalised HT-PBP2B intensities for mature Z-rings only at t=0 min showing whether they*
187 *continued dividing (blue) or not (red). Inset:* Percentage of cells that continued dividing classified by HT-PBP2B signal. Low
188 2B: intensity<0.15, high 2B: intensity>0.15. Scale bars: 500 nm. Numbers above stacked bars indicate number of cells.

189 We used rapid arrest of FtsZ treadmilling by PC19 to investigate the role of FtsZ treadmilling
190 throughout cell division. We imaged cells in fast growth conditions (rich media, 37°C) using a
191 commercial microfluidic device with continual fluid flow both before and during treatment with excess
192 PC19 (Figure 3, Methods). Treatment with PC19 prevented Z-rings in earlier stages of division from
193 continuing to divide, but Z-rings in later stages continued dividing (Figure 3a-b, Supplementary Videos
194 10-13). PC19 treatment prevented nascent Z-rings from condensing into mature Z-rings or constricting
195 (N=86; Figure 3b, Supplementary Figure 8). Furthermore, we found that treatment prevented 53%
196 (N=89) of mature Z-rings from beginning constriction, while only 10% (N=52) of initially constricting Z-
197 rings were prevented from continuing constriction. In contrast, treatment with PenG inhibited
198 constriction altogether (Supplementary Video 14). Similar results were observed in slow growth
199 conditions (poor media, 30°C; Supplementary Figure 9, Supplementary Video 15). Together these data
200 show that FtsZ treadmilling is required for the condensation of filaments from a nascent to a mature
201 Z-ring, but becomes dispensable at some point during the mature Z-ring stage.

202 We wondered what events within the mature Z-ring stage corresponded to this change in
203 dispensability of FtsZ treadmilling. Divisome assembly in *B. subtilis* is approximately a two-step process

204 where FtsZ and other cytoplasmic proteins arrive first, followed by arrival of the PG synthesis
205 machinery just before constriction initiation, including the septal transpeptidase PBP2B[20]. To
206 determine when FtsZ treadmilling becomes dispensable within mature Z-rings, we repeated the
207 treadmilling inhibition assay using a strain expressing both FtsZ-GFP and HaloTag-PBP2B from
208 inducible exogenous promoters (SH212, Methods). This strain showed the same response overall to
209 PC19 treatment as before (Supplementary Figure 10, Supplementary Videos 16-17). For mature rings
210 we found that the amount of PBP2B present at time of FtsZ treadmilling arrest correlated strongly
211 with whether rings would constrict or not (Figure 3c-d). Similar results were obtained for a functional
212 mNeonGreen-PBP2B fusion expressed from the native locus[1] (ME7 Supplementary Video 18,
213 Supplementary Figure 11). The FtsZ-GFP signal also increased during the mature ring stage, but unlike
214 PBP2B the FtsZ signal was only weakly correlated with the percentage of cells completing division
215 (Supplementary Figure 10b). FtsZ treadmilling thus becomes dispensable for cell division just after the
216 arrival of the PG synthesis machinery. These results are consistent with previous findings in *S. aureus*
217 that FtsZ treadmilling is required until constriction has initiated, and thereafter becomes dispensable[3].
218 Since we previously observed that FtsZ treadmilling guides processive septal synthesis[1], we conclude
219 that FtsZ treadmilling in mature Z-rings likely functions by guiding septal synthases during the earliest
220 stages of septal synthesis, before a septum has been formed.

221 Together, our data reveal two essential functions for FtsZ treadmilling in division. The first is a novel
222 peptidoglycan synthesis-independent function, to condense sparse FtsZ filaments into a dense Z-ring.
223 The second function is to initiate constriction by guiding initial cell-wall synthesis.

224 **FtsZ treadmilling accelerates constriction**

225 We wondered how to reconcile the finding that FtsZ treadmilling is dispensable for constriction after
226 initiation, with our previous observation that FtsZ treadmilling sets the rate of constriction[1]. To
227 address this, we set out to determine the effect of rapid, total arrest of FtsZ treadmilling on the septal
228 constriction rate. In order to precisely measure constriction rates immediately after PC19 treatment,
229 we developed a physical model for Gram-positive septal constriction which could be fitted to partial
230 septal constriction trajectories immediately after cell treatment with PC19 (Methods, Supplementary
231 Note 2, Figure 4a). For comparison to previous observations we converted the observed constriction
232 rates of partially constricted cells to an effective constriction time t_{eff}, the total amount of time it would
233 take for an average septum to constrict completely (Methods).

234 We observed that the constriction time of untreated cells in fast growth conditions was 15.3 min, IQR
235 13.5-17.9 (N=765, Figure 4b). FtsZ treadmilling inhibition by PC19 treatment caused a robust 7.7 min,
236 95% CI [7.1,8.3] (N=419), increase in constriction time for cells grown in rich media. This is similar to
237 the increase in constriction time caused by high expression of a GTP-hydrolysis-impaired FtsZ-D213A
238 mutant (Supplementary Figure 13). Fluorescent PBP2B signal continued to increase after treatment
239 with PC19 (Supplementary Figure 12), indicating that the reduced constriction rate is unlikely to be
240 caused by indirect reduction of synthase levels at the septum. These results show that although FtsZ
241 treadmilling is not required for septal PG synthesis after constriction initiation, treadmilling promotes
242 efficient constriction by increasing septal constriction rate.

243

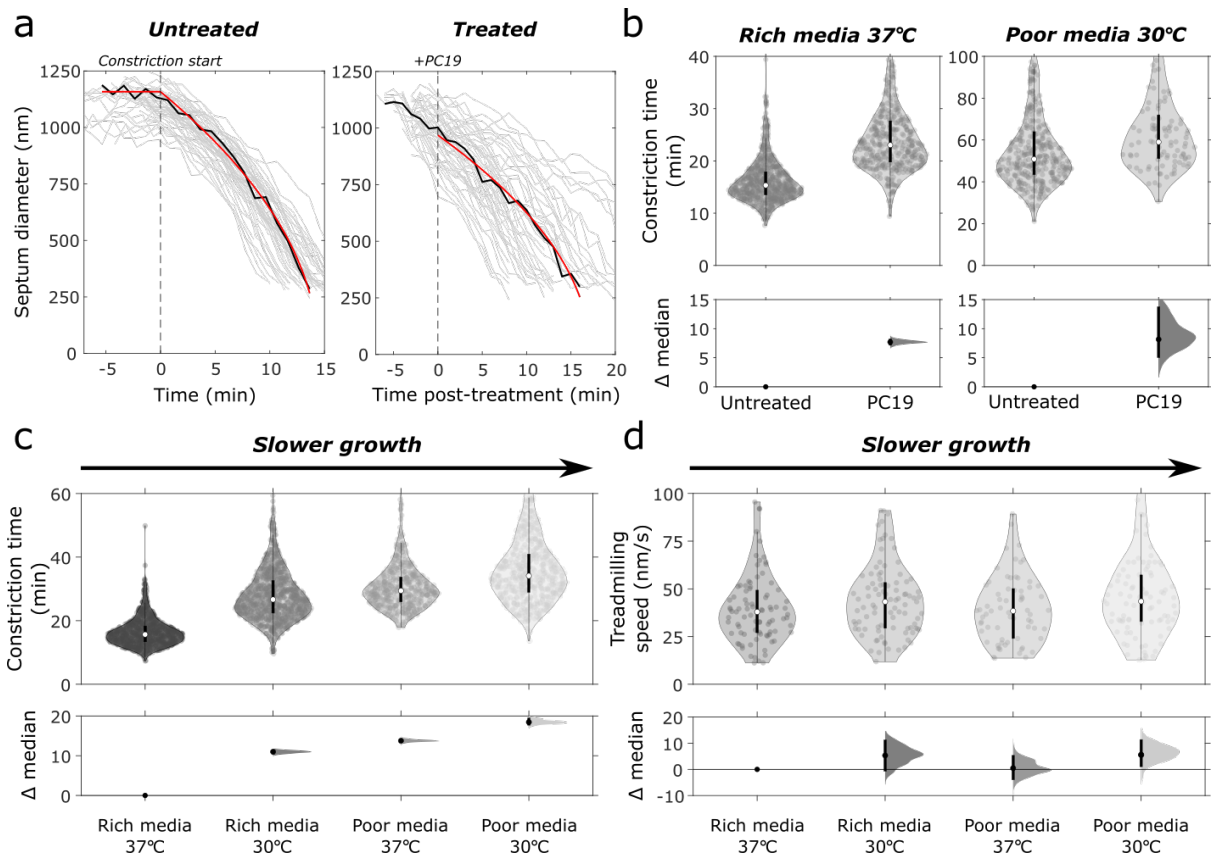

Figure 4. Constriction rate is accelerated by FtsZ treadmilling and fast cell growth rate. *(a) Time traces of ring diameters from mNeonGreen-PBP2B strain (ME7) for untreated (left) and PC19-treated (right) cells with constant PG synthesis model (red) fitted to representative traces (black).* Untreated cell trajectories are aligned relative to fitted constriction start time. PC19-treated cell trajectories are aligned relative to the arrival time of PC19-laced media. *(b) Constriction time before and after PC19 treatment for both fast growth (rich media 37°C) and slow growth (poor media, 30°C) conditions. (c) Constriction time of mNeonGreen-PBP2B cells in rich and poor media at two growth temperatures. (d) FtsZ-mNeonGreen (bWM4) treadmilling speeds in different media and temperature. Top panels, b-d:* violin plots; white circle, sample median; error bars, interquartile range. *Bottom panels, b-d: Bottom panels:* DABEST plots showing effect size analysis, compared to leftmost condition; black circles, median difference; error bars, 95 % confidence interval of median difference.

Cell growth rate limits septal constriction rate independently of FtsZ treadmilling

Growth rate and cell size for most bacterial species are linked to nutrient availability and culture temperature[21]. We sought to identify how growth rate affects the constriction rate of *B. subtilis* cells. We measured the constriction rate under varying temperature and nutrient availability conditions using a strain expressing PBP2B from its native promoter fused to mNeonGreen (ME7, Methods). Slower growth in either minimal media or at low temperature led to correspondingly longer constriction times (Figure 4a). We determined FtsZ treadmilling speed for all conditions using a dilute exogenous label of FtsZ-mNeonGreen (bWM4) which shows no growth or morphology phenotype at 37°C[1]. FtsZ treadmilling speed was constant across all growth conditions tested (Figure 4b), showing that the effect of growth rate on septal constriction is independent of FtsZ treadmilling.

We next investigated whether FtsZ treadmilling also promotes constriction in slow growth conditions. As in fast growth conditions, arresting FtsZ treadmilling increased the constriction time (Figure 4b, Supplementary Video 19). However, the relative increase in constriction time was much lower in slow growth conditions (1.16-fold [1.06,1.27] vs 1.50-fold [1.44,1.57] change). These observations show that cell growth rate is a major rate-limiting step for active septal constriction, with treadmilling FtsZ filaments acting as a secondary promotor of septal synthesis.

DISCUSSION

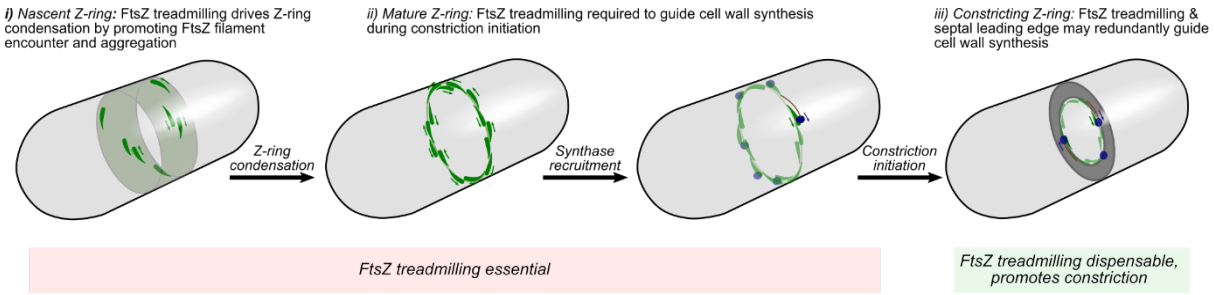

Figure 5: Model for function of FtsZ treadmilling in Z-ring assembly and septal constriction.

Using bespoke ultra-sensitive microscopy of cell division protein dynamics, we discovered that FtsZ treadmilling plays two separate essential roles in cell division: to establish the mature divisome by condensing diffuse filaments into a dense ring, and to guide septal constriction initiation (Figure 5).

We found that condensation of sparse FtsZ filaments into a dense Z-ring is required for cell division. Using VerCINI microscopy we observed that motile FtsZ filaments frequently collide and aggregate in nascent Z-rings. Furthermore, chemical arrest of treadmilling completely abolished FtsZ ring condensation. Attractive lateral interactions between FtsZ filaments, via the FtsZ C-terminal-linker and cytoplasmic FtsZ-associated proteins are known to mediate FtsZ bundling and Z-ring condensation[22–26]. Our results reveal an additional key factor in assembling the Z-ring: FtsZ filament treadmilling drives filament interactions by enabling FtsZ filaments to rapidly search the mid-cell surface and efficiently encounter one another. We conclude that FtsZ treadmilling and FtsZ lateral interactions together drive aggregation of FtsZ filaments into a condensed Z-ring. This is remarkably reminiscent of motility-driven partitioning of FtsZ filaments into higher-order structures previously observed *in vitro*[9,27].

The second role of FtsZ treadmilling is to guide septal PG synthesis. We found that this role is essential in the constriction initiation phase of *B. subtilis* cell division, but dispensable afterwards. Together with our previous observations that FtsZ treadmilling guides individual synthase molecules during PG synthesis[1], it is likely that during constriction initiation FtsZ filament treadmilling is required to guide the synthases around the circumference of the mid-cell in the absence of an established septum. We also observed that FtsZ treadmilling dynamics are cell cycle regulated, with Z-ring condensation promoting efficient FtsZ treadmilling. In addition to concentrating the division machinery into a small area, Z-ring condensation may indirectly promote efficient constriction initiation by increasing the fraction of treadmilling filaments available to guide cell-wall synthesis.

Although FtsZ treadmilling is dispensable after constriction initiation, we found that treadmilling increases the rate of septal constriction. We found that overall cell growth rate has a much stronger effect on septal constriction rate than FtsZ treadmilling. We conclude that FtsZ treadmilling plays only a secondary role in active constriction, while its critical roles occur prior to constriction initiation. After constriction initiation, the highly ordered septal leading edge[28] may be sufficient to act as a guide for processive septal PG synthesis, with FtsZ filaments acting as a mid-cell localiser and redundant guide during active constriction.

The VerCINI method presented here is a powerful tool for ultra-sensitive measurement of cell division protein dynamics and mode of action of cell division targeting antibiotics. We anticipate that many other bacterial structures, especially the bacterial cell envelope and associated proteins, could also benefit from VerCINI's high resolution top-down cell view.

A key puzzle in bacterial cell biology is how nanoscale division proteins spontaneously and accurately build a micron-size wall at mid-cell. Treadmilling gives FtsZ filaments the remarkable ability to

autonomously drive their own circumferential motion around the mid-cell surface. Our results show that the self-driving capability of FtsZ filaments is crucial to solving the scale problem of cell division by directing divisome assembly and initial septal synthesis to a narrow band around the mid-cell, laying the template for septum construction. Dynamic, self-organizing FtsZ filaments thus provide long-distance order and collective motion around the bacterial mid-cell in the absence of cytoskeletal motor proteins.

ACKNOWLEDGEMENTS

We thank Henrik Strahl (Newcastle) for helpful discussions, Ling Wu and Jeff Errington (Newcastle) for strains and antibodies, and Ethan Garner (Harvard) for strains. SH, KW, CJ and EK acknowledge funding support by a Newcastle University Research Fellowship and a Wellcome Trust & Royal Society Sir Henry Dale Fellowship grant number 206670/Z/17/Z. NT supported by a UK Engineering and Physical Sciences Research Council doctoral studentship. RH and PA funded by grants from the UK Biotechnology and Biological Sciences Research Council (BB/M022374/1), the UK Medical Research Council (MR/K015826/1), and Wellcome Trust (203276/Z/16/Z). CD and KW acknowledge funding support by ERC grant SynDiv (669598) and the Netherlands Organisation for Scientific Research (NWO/OCW) as part of the Frontiers of Nanoscience and Basyc programs.

AUTHOR CONTRIBUTIONS

KW, CJ and NT acquired data. KW, CJ, NT and SH analysed data. KW, CJ, SH and CD developed the VerCINI method. KW performed nanofabrication, supervised by CD. SH, KW, PA and RH wrote software. CJ, EK, NT created and characterised bacterial strains. SH and CD directed the research. KW, SH and CJ wrote the manuscript with input from all authors.

330 ## MATERIALS AND METHODS

331 **Bacterial strains and growth conditions**

332 Strains used in this study are listed in Supplementary Table 1. Strains were streaked from -80°C freezer
333 glycerol stocks onto Nutrient Agar (NA) plates containing the relevant antibiotics and/or inducers and
334 grown overnight at 37°C. Single colonies were transferred to liquid starter cultures in either Time-
335 Lapse Medium (TLM[30]) or PHMM media and grown with agitation at 200 rpm overnight at either 30°C
336 (TLM) or 22°C (PHMM[1]). The next day, TLM starter cultures were diluted to a starting OD_{600} of 0.1 in
337 Chemically-Defined Medium (CDM[30]), while PHMM starter cultures were diluted to a starting OD_{600} of
338 0.05 in PHMM, and these liquid cultures were grown at 30°C or 37°C with any required inducer until
339 they reached the appropriate OD_{600}. When necessary, antibiotics and inducers were used at the
340 following final concentrations: chloramphenicol 5 µg/ml, spectinomycin 60 µg/ml, erythromycin
341 1 µg/ml, lincomycin 10 µg/ml, kanamycin 5 µg/ml, xylose 0.08% and IPTG 20 µM.

342 **Strain construction**

343 **SH211:** (PY79 Δ*hag*) Strain SH211 was constructed by transforming competent PY79 with genomic
344 DNA extracted from strain PB5250, using standard protocols[31]. The antibiotic resistance cassette was
345 removed using pDR224 as described previously[32].

346 **SH130:** (PY79 Δ*hag ftsZ::ftsZ-cam*) Strain SH130 was constructed by transforming SH211 competent
347 cells with genomic DNA extracted from strain PAL642

348 **SH212:** (PY79 *pbp2B::erm*-$P_{hyperspank}$-*HaloTag-15aa-pbp2B* Ω *amyE::spc* P_{xyl} *gfp-ftsZ*) Strain SH212 was
349 constructed by transforming competent bGS28 cells with genomic DNA extracted from strain 2020.

350 All published strains are available on request to the authors.

351 **Bacterial strain characterization**

352 Strains were characterised by cell morphology analysis (Supplementary Figure 2). FtsZ-GFP protein
353 levels were determined by Western blotting (Supplementary Figure 1).

354 **Cell morphology analysis**

355 PY79 and SH130 cultures were prepared for imaging in CDM or PHMM as described above. Once the
356 cultures had reached OD_{600} 0.4-0.5, Nile Red was added to 200µl of cells to a working concentration
357 of 1 µg/ml, and incubated at growth temperatures for 5 mins, prepared on agarose microscope slides
358 as described below and cell morphology images recorded. Cell length was then manually determined
359 using ImageJ.

360 **Western blotting**

361 PY79 and SH130 cultures were grown overnight in 2ml LB at 30°C. The following morning, cultures
362 were diluted to ~OD_{600} 0.05 and grown at 30°C until ~OD_{600} 0.6. Cultures were centrifuged at 13,000
363 rpm for 2 minutes and the pellets resuspended in 104µL PBS plus peptidase inhibitor (Roche
364 cOmplete™, Mini Protease Inhibitor Cocktail). Cells were then sonicated and 4X Laemmli Buffer and
365 Dithiothreitol (DTT) added. Samples were heated at 80°C for 10 minutes, following which the cells
366 were centrifuged for 5 minutes at 14000 rpm. 20µL lysates were then separated by SDS PAGE in 4-
367 12% Bis-Tris gels and blotted onto 0.45µm PVDF membrane. Primary antibodies against FtsZ (anti-
368 rabbit) were coupled with HRP-conjugated polyclonal antibodies (anti-rabbit, Sigma). Samples were
369 developed using Pierce™ ECL Western Blotting Substrate (Thermofisher) and imaged using an
370 ImageQuant LAS 4000 mini Biomolecular Imager (GE Healthcare).

371 **Microscopy**

372 Power density, exposure time and other key parameters are listed for each microscopy experiment in
373 Supplementary Table 4. All imaging was done using either a Nikon N-SIM/N-STORM inverted
374 fluorescence microscope (Figure 4, Supplementary Figure 14) or a custom-built inverted microscope
375 (otherwise).

376 *Nikon N-STORM.* Cells were illuminated with a 488 nm line from an Argon Ion laser (CVI Melles-Griot).
377 A 100x TIRF objective (Nikon CFI Apochromat TIRF 100XC Oil) was used for imaging and an Andor iXon
378 DU897 EMCCD camera was used, with a 1.5 x OptoVar (Nikon) and standard Nikon tube lens, giving
379 an effective image pixel size of 106 nm/pixel. Cells were illuminated via HiLO[33] inclined illumination to
380 minimise background using an objective TIRF module (Nikon N-STORM module) using 488 nm laser
381 excitation.

382 *Custom microscope.* Cells were illuminated with a 488 nm laser (Obis) and/or a 561 nm laser (Obis) as
383 indicated. A 100x TIRF objective (Nikon CFI Apochromat TIRF 100XC Oil) was used for all experiments
384 except microfluidic VerCINI measurements where a 100x silicone immersion objective (CFI SR HP Plan
385 Apochromat Lambda S 100XC Sil, Nikon) was used for deep focusing. A 200 mm tube lens (Thorlabs
386 TTL200) and Prime BSI sCMOS camera (Teledyne Photometrics) were used for imaging, giving effective
387 image pixel size of 65 nm/pixel. Imaging was done with a custom-built ring-TIRF module operated in
388 ring-HiLO[33] using a pair of galvanometer mirrors (Thorlabs) spinning at 200 Hz to provide uniform, high
389 SNR illumination.

390 **Nanofabrication**

391 Micropillars were patterned using electron-beam lithography and etched using reactive-ion etching.
392 Briefly, a silicon wafer was spin coated with AR-N 7700.18 (Allresist GmbH). Features were patterned
393 using a Leica EBPG 5000+ with 56 nm beam step size. The unexposed resist was removed with solvent
394 Microposit MF-321 and the exposed wafer surface was etched using an AMS Bosch etcher. The
395 remaining resist was removed using oxygen plasma. Pillars widths ranged from 1.0 to 13 µm with
396 height 6.7 µm, spaced 5 µm apart. Final micropillar dimensions were confirmed using SEM.

397 Micropillar wafers were silanised to allow cured polydimethylsiloxane (PDMS) to be removed without
398 damaging structures. To do this, wafers were coated with (tridecafluoro-1,1,2,2-tetrahydrooctyl)
399 trichlorosilane (abcr GmbH) by vapour deposition.

400 **VerCINI**

401 Agarose microholes were formed by pouring molten 6% agarose onto the silicon micropillar array.
402 Patterned agarose was transferred into a Geneframe (Thermo Scientific) mounted on a glass slide, and
403 excess agarose was cut away to ensure sufficient oxygen. Cells at $OD_{600} \sim 0.4$ were concentrated 100x
404 by centrifugation and added onto the agarose pad. Cells were then loaded into the microholes by
405 centrifuging the mounted agarose pad with concentrated cell culture in an Eppendorf 5810 centrifuge
406 with MTP/Flex buckets. Unloaded cells were rinsed off with excess media.

407 FtsZ treadmilling dynamics were imaged at 1 frame/s (continuous exposure) for 2 mins at 1-8 W/cm^2.
408 After each field of view was imaged, a multi-slice Z-stack was taken at 500nm intervals to exclude
409 tilted or improperly trapped cells, in addition to excluding Z-rings that have an adjacent Z-ring 1µm
410 above or below the imaging plane. VerCINI experiments were performed on cells in a *Δhag* mutant
411 background, preventing undesirable cell rotation within the microholes by disabling flagellar motility.

412

413 **Microfluidic VerCINI**

414 *Device assembly*

415 Open-topped microhole coverslips were formed from PDMS using the silicon micropillar array
416 (Supplementary Figure 15). All PDMS reagents and processing equipment were from BlackHoleLab.
417 PDMS elastomer base and curing agent were mixed in a 1:1 ratio and degassed. The degassed mixture
418 was then poured on top of the microhole array and a microscope coverslip was pressed down to form
419 a thin layer. PDMS was cured by baking at 80°C for 1 hr, and the coverslip with patterned PDMS layer
420 was removed from the silicon mould.

421 Microfluidic chambers were prepared using readily-available components (Supplementary Figure 15).
422 First, holes were drilled into a glass microscope cover slide using a diamond drill bit (Kingsley North).
423 A flow channel was then made by cutting a strip of double-sided tape using either a scalpel or laser
424 engraver. One side of the double-sided tape was then adhered to the microscope cover slide. Cut
425 pipette tips were then inserted into the drilled holes, and polyethylene tubing (Smiths Medical) was
426 inserted into them. Leakage was prevented by sealing pipette tips and tubing using epoxy.

427 To load cells into the microholes, PDMS was first rendered hydrophilic by treating with air plasma for
428 3 min. A 9 mm diameter silicone gasket (Grace Bio-Labs) was then placed over the PDMS microholes.
429 Cells at $OD_{600} \sim 0.4$ were concentrated 100x by centrifugation and pipetted into the silicone gasket.
430 Cells were then loaded into the microholes by centrifuging the microhole-containing coverslip with
431 concentrated cell culture in an Eppendorf 5810 centrifuge with MTP/Flex buckets. The coverslip was
432 covered during centrifugation to prevent evaporation. Unloaded cells were rinsed off with excess
433 media. To ensure adequate loading, this loading-and-rinsing protocol was then repeated.

434 After cells were loaded into microholes, the silicone gasket was removed and the flow chamber was
435 fully assembled by adhering the PDMS-covered coverslip to the exposed side of double-sided tape on
436 the glass cover slide (Supplementary Figure 15).

437 *Imaging*

438 Due to the relatively thick (~50 µm) layer of PDMS between the coverslip surface and the confined
439 cells, a Nikon silicone immersion objective (CFI SR HP Plan Apochromat Lambda S 100XC Sil, Nikon)
440 was used for imaging due to its high working distance (0.3 mm).

441 Since the indices of refraction for PDMS and aqueous solution are similar, autofocusing systems relying
442 on the reflection of an IR signal from two interfaces were not adequate due to weak signal. Instead,
443 autofocusing was done using an image-based approach first described by McGorty and co-workers[19]
444 using cross-correlation of brightfield images. Briefly, a separate brightfield imaging pathway was
445 added to the microscope using a 1050 nm IR LED (Thorlabs) and IR-sensitive camera (UI-1220LE-M-GL,
446 Imaging Development Systems GmbH), and a plugin for Micro-Manager was developed to calculate
447 cross-correlations and move the sample stage (https://github.com/HoldenLab/DeepAutoFocus). At
448 the start of an experiment, a z-stack of IR brightfield images was obtained as a reference. During the
449 experiment, the cross-correlation map between every new IR brightfield image and this reference
450 stack was calculated, and the sample stage was moved to compensate for any drift. To our knowledge
451 this is the first application of IR cross-correlation autofocusing to live cell imaging.

452 *Fluid control*

453 Media was flowed through the chamber by a syringe pump (Aladdin-220, World Precision
454 Instruments). To prevent potential leakage, media was pulled through the chamber from fluid

455 reservoirs by operating the syringe pump in withdraw mode. Complete solution exchange occurred
456 within 7 s of initial compound arrival time, estimated using a rhodamine tracer.

457 **CellASIC experiments**

458 The microfluidic CellASIC system (EMD Millipore) was used to image constricting cells during
459 treatment with division inhibitors. Cells were loaded into B04A plates and equilibrated in blank media
460 for ~15 min with a pressure of 2 psi (~6 µL/hr flow rate) prior to imaging.

461 In a typical experiment, untreated constricting cells were imaged for 30 min (1 min/frame, 1 s
462 exposure, 1-2 W/cm^2) while blank media was flowed using 2 psi. Solution exchange was done by first
463 flowing media with compound using 8 psi (~34 µL/hr flow rate) for 15 s, then dropping the pressure
464 to 2 psi for the remainder of the experiment (50-90 min). DMSO treatment alone caused a small but
465 robust increase in constriction time (Supplementary Figure 16). However, pre-adaptation of cells to
466 blank media containing DMSO eliminated this effect, showing that observed effects of PC19 treatment
467 resulted from the drug and not the solvent that accompanied it (Supplementary Figure 16).

468 The arrival time of the compound at the cells was most estimated by treating the FtsZ-GFP strain with
469 10 µM PC19 using our standard flow protocol. PC19 causes the diffuse cytoplasmic FtsZ-GFP to rapidly
470 polymerise into short filaments throughout the cell (Supplementary Videos 10-13), providing a clear
471 signal for compound arrival. From these experiments we determined that compound arrives 3-4 min
472 after fluid exchange.

473 **Microscopy of horizontal cells**

474 *Sample preparation*

475 Coverslips were first cleaned by treating with air plasma for 5 min. Slides were prepared as described
476 previously[30]: Flat 2% agarose pads of either CDM or PHMM were prepared inside Geneframes (Thermo
477 Scientific) and cut down to strips of 5 mm width to ensure sufficient oxygen supply to cells. Cell
478 cultures were grown to OD_{600} between 0.2 and 0.4, when 0.5 µL of cell culture was spotted on the
479 pad. Cells were allowed to adsorb to the pad for 30 s before a plasma-cleaned coverslip was placed
480 on them. After spotting on agarose pads, cells were allowed to equilibrate within the microscope body
481 for 15 min before being imaged. Cells were then imaged either by TIRF microscopy for observation of
482 FtsZ filament dynamics, or ring-HiLO for time-lapse observation, with experimental parameters
483 defined in Supplementary Table 4.

484 **Image analysis**

485 ***VerCINI data analysis***

486 *Pre-processing*

487 Videos were denoised using the ImageJ plugin PureDenoise[17], which is based on wavelet
488 decomposition. Key assumptions of the method are (i) local spatiotemporal similarity within the
489 image (ii) absence of sharp discontinuities, guaranteed by diffraction-limited nature of the image. The
490 denoising algorithm makes does not make any assumptions on the type of underlying biological
491 structure.

492 Denoised videos were registered using the ImageJ plugin StackReg[34]. Image stacks of vertically
493 immobilised cells were inspected to exclude tilted cells or out of focus FtsZ-rings, or FtsZ rings where
494 a second Z-ring was closer than 1 um to the focal plane. Cropped region of interest movies containing
495 single in-focus cells were manually selected and exported for analysis. An ImageJ package for VerCINI
496 data processing is available (https://github.com/HoldenLab/Ring_Analysis_IJ).

VerCINI background subtraction, kymograph extraction, quantification

Custom software for quantitative cytoplasmic background subtraction and kymograph extraction was developed for analysis of VerCINI movies (https://github.com/HoldenLab/ring-fitting2). Fluorescence images of isolated vertical cells were fitted to a joint explicit model for diffuse out-of-focus cytoplasmic background (Gaussian + Cauchy model) plus septal protein signal, modelled as a 12 sectored annulus with each sector of variable amplitude.

$$F(x,y) = Signal(x,y) + Bg(x,y)$$

Signal is calculated in polar coordinates, around the septal ring centre fit parameter (x_0, y_0), and then transformed into Cartesian coordinates. Signal is defined as

$$S(r,\theta) = A_i(\theta)\exp\left(-\frac{(r-R_0)^2}{2\sigma^2}\right),$$

where $A_i(\theta)$ defines a 12 sectored ring. Background is defined as

$$Bg(x,y) = a\exp\left(\frac{-((x-x_0)^2+(y-y_0)^2)}{2\sigma_{bg1}^2}\right) + b\frac{\sigma_{bg2}^2}{(x-x_0)^2+(y-y_0)^2+\sigma_{bg2}^2} + c.$$

This explicit model allowed accurate sub-pixel location of a circular line profile at the septal leading edge. Explicit subtraction of complex background signal also allowed septal intensity quantification. The background subtracted intensity along the circular line profile was then calculated for each frame and automatically plotted as a kymograph. Kymographs were plotted over the [0,720°] ie two complete revolutions around the line profile for ease of visualization, specifically to allow straightforward visualization of motile filaments crossing the 360°,0° boundary. For each cell, the Z-ring diameter was determined from the fitted model in the kymograph extraction step. Median septal intensity was calculated as the median value of all kymograph pixels from the first 60 image frames.

FtsZ filament treadmilling analysis using VerCINI

We found that automated methods for in vitro FtsZ filament speed measurements, either after Dos Santos Caldas and coworkers[35] or using a similar in-house algorithm, are currently insufficient for FtsZ filament speed analysis in either horizontal or vertical cells compared to manual analysis, because at cellular filament density they currently perform poorly at detecting static filaments , break the complete trajectories of motile filaments into multiple shorter trajectories, and cannot reliably process images from dense Z-rings in horizontal cells.

We therefore performed manual measurement of filament speed and processivity by kymograph analysis, annotating filaments as lines in ImageJ and then measuring the angle via ImageJ script. As the intensity range across kymographs is large, manual detection and analysis of filaments was aided by applying a ridge filter[36] to the kymograph which detects ridges in the image, independent of absolute intensity. The ridge filter consists of a Gaussian blur operation to set the feature scale and suppress noise (here 2 pixels, 130 nm), followed by calculation of the major eigenvalue of the Hessian matrix for each pixel, implemented as an ImageJ macro in the package listed above. Joint annotation of the ridge filtered and raw intensity kymograph was performed, allowing sensitive annotation of both bright and dim filaments (Supplementary Figure 17).

Horizontal cell image analysis

Pre-processing.

Images were denoised and registered as described above.

536 *Cell segmentation and tracking of division protein localization.*

537 MicrobeJ[11] was used to track individual FtsZ-/PBP2B-rings and export their centroid coordinates for
538 analysis. To do this, image backgrounds were first subtracted using a sliding paraboloid window of 50
539 pixels and all frames were converted to 8-bit for easier thresholding.

540 Two approaches were used to identify division protein localization, depending on the experiment. For
541 measurements of septal constriction rate only (Figure 4a), which requires only detection of bright
542 dense FtsZ/PBP2B rings, a simple approach of intensity-based threshold detection was applied in
543 MicrobeJ a threshold was selected manually for each field of view using MinError. Additional area and
544 length thresholds (Area: [0.08 Inf] μm^2, Length: [0.02 1.8] µm) were established to exclude objects in
545 fields of view that were not rings. Tracks shorter than 7 frames were excluded. Data was then exported
546 for analysis in MATLAB.

547 For analysis of FtsZ ring dynamics over the entire division process, from nascent Z-ring assembly to
548 late constriction (Figure 1), it was necessary to additionally robustly detecting diffuse patchy FtsZ-
549 rings. We trained the machine learning segmentation tool Ilastik[12] to detect cell outlines with
550 fluorescence images of cells labelled with FtsZ. For detection of diffuse Z-rings, we applied a large
551 Gaussian blur filter to the images, and then multiplied this by the Ilastik-segmented binary image,
552 which had the effect of separating any overlap of Z-rings between adjacent cells. Intensity threshold-
553 based detection of Z-rings was then performed in MicrobeJ as above.

554 *Quantification of division protein septal localization*

555 Custom MATLAB software was developed to measure the diameters and intensities of Z- and 2B-rings
556 obtained from either MicrobeJ or Ilastik. Each frame of each individual ring was first segmented using
557 a multi-level threshold to distinguish the septum, cytoplasm, and background. The septal axis and the
558 cell axis were identified using the segmented image, and the image was rotated such that pixels were
559 aligned along these axes. Line profiles of Z- and 2B-rings were obtained by averaging pixel values along
560 the septal axis ±2 pixels to reduce noise. Diameter were then obtained by fitting line profiles to a toy
561 model that describes a circle of uniform intensity rotated to be orthogonal to the axis of the imaging
562 plane ('Tilted Circle Model', Supplementary Note 1, Supplementary Figure 18). Septal density was
563 calculated as the total intensity along the lateral line profile, divided by the ring circumference, as
564 calculated from the constriction rated analysis (below) to reduce single frame noise. Septal density
565 was used in place of total intensity, in order to compare to the septal intensity measurements
566 obtained during the VerCINI exerpiments. Axial thickness was estimated by fitting an axial line profile
567 to an analytical super-Gaussian and calculating the full-width half maximum.

568 *FtsZ filament treadmilling analysis from TIRF microscopy data*

569 Images were denoised and registered as above. TrackMate[37] was used to help identifying treadmilling
570 FtsZ filaments outside of dense Z-rings. A line region of interest (ROI) was drawn perpendicular to the
571 cell axis where treadmilling filaments were identified. Kymographs were calculated along this line
572 profile FtsZ filaments trajectories in the kymograph were marked with a line ROI (Supplementary
573 Figure 14). Treadmilling speed for each filament trajectory was calculated from the angle of the line
574 ROIs.

575 ***Constriction rate analysis***

576 Previous models for septal constriction have either been *ad hoc*[26] or tailored to Gram-negative cell
577 division based on remodelling of a hemispherical cap[27]. We derived a simple model for Gram-positive
578 constriction, assuming (i) outside-in synthesis of a flat plate at mid-cell and (ii) total PG synthesis rate
579 around the septal leading edge is constant (Supplementary note 2)

$$d(t) = \begin{cases} d_0, & t < t_0 \\ \sqrt{d_0^2 - \frac{4k}{\pi}(t - t_0)}, & t \geq t_0 \end{cases}$$

Where d_0 is the initial Z- or 2B-ring diameter, t_0 is the time constriction begins, and k is the rate at which area is added to the septal plate. This model fitted measured constriction trajectories well, and the estimated time of constriction completion corresponded closely to completion times independently estimated from PBP2B departure in wild type cells (Supplementary Figure 19).

We measured constriction rates in the mNeonGreen-PBP2B strain, since FtsZ-GFP mislocalises post-treatment with PC19 and makes it difficult to track large numbers of septa. A small amount of mNeonGreen-PBP2B signal remained at mid-cell after constriction had finished. This excess signal was excluded from the rate analysis by cutting the 2B-ring data after this drop in intensity. We obtained constriction time distributions for PC19-treated cells by fitting only to post-treatment data.

For comparison to previous observations we converted the observed constriction rates to an effective constriction time t_{eff}, the total amount of time it would take for an unconstricted septum to constrict completely (Methods) given the fitted rate k : $t_{eff} = 2\pi \cdot \frac{d_0^2}{k}$. The average diameter of the unconstricted septum d_0 was estimated as 1100 ± 100 nm (mean, SD) for the mNeonGreen-PBP2B based on the background fluorescence signal in the cell.

Statistics

Data were analysed using estimation statistics, which focusses on magnitude and robustness of effect size, rather than significance testing, using DABEST[38] (Data Analysis with Bootstrap Coupled Estimation). Averages reported were median values unless otherwise indicated. All effect size estimates were calculated based on difference of medians. 95% confidence interval of the median, or of the difference of medians, was estimated by bootstrapping (**https://github.com/HoldenLab/violinplusDABEST-Matlab**) and indicated with square brackets []. Interquartile range was indicated by IQR. Thick error bar lines in Violin plots indicate interquartile range, thin lines indicate adjacent vales. Error bars in DABEST plots indicate 95% CI of median difference, estimated by bootstrapping. Sample size, indicating number of filaments/Z-ring, cells, microscope fields of view, technical and biological replicates, as appropriate, is presented for each dataset in Supplementary Table 3.

CODE AVAILABILITY

Custom software is available on the Holden lab GitHub page:

https://github.com/HoldenLab/Ring_Analysis_IJ
https://github.com/HoldenLab/ring-fitting2
https://github.com/HoldenLab/DeepAutoFocus

612 **REFERENCES**

613 1. Bisson-Filho, A. W. *et al.* Treadmilling by FtsZ filaments drives peptidoglycan synthesis and
614 bacterial cell division. *Science* **355**, 739–743 (2017).
615 2. Yang, X. *et al.* GTPase activity–coupled treadmilling of the bacterial tubulin FtsZ organizes
616 septal cell wall synthesis. *Science* **355**, 744–747 (2017).
617 3. Monteiro, J. M. *et al.* Peptidoglycan synthesis drives an FtsZ-treadmilling-independent step of
618 cytokinesis. *Nature* (2018) doi:10.1038/nature25506.
619 4. Perez, A. J. *et al.* Movement dynamics of divisome proteins and PBP2x:FtsW in cells of
620 Streptococcus pneumoniae. *Proc. Natl. Acad. Sci.* **116**, 3211–3220 (2019).
621 5. Baranova, N. *et al.* Diffusion and capture permits dynamic coupling between treadmilling FtsZ
622 filaments and cell division proteins. *Nat. Microbiol.* **5**, 407–417 (2020).
623 6. Yao, Q. *et al.* Short FtsZ filaments can drive asymmetric cell envelope constriction at the onset
624 of bacterial cytokinesis. *EMBO J.* e201696235 (2017) doi:10.15252/embj.201696235.
625 7. Strauss, M. P. *et al.* 3D-SIM Super Resolution Microscopy Reveals a Bead-Like Arrangement
626 for FtsZ and the Division Machinery: Implications for Triggering Cytokinesis. *PLoS Biol* **10**, e1001389
627 (2012).
628 8. Holden, S. J. *et al.* High throughput 3D super-resolution microscopy reveals *Caulobacter*
629 *crescentus* in vivo Z-ring organization. *Proc. Natl. Acad. Sci.* **111**, 4566–4571 (2014).
630 9. Loose, M. & Mitchison, T. J. The bacterial cell division proteins FtsA and FtsZ self-organize into
631 dynamic cytoskeletal patterns. *Nat. Cell Biol.* **16**, 38–46 (2014).
632 10. Levin, P. A., Kurtser, I. G. & Grossman, A. D. Identification and characterization of a negative
633 regulator of FtsZ ring formation in Bacillus subtilis. *Proc. Natl. Acad. Sci.* **96**, 9642–9647 (1999).
634 11. Ducret, A., Quardokus, E. M. & Brun, Y. V. MicrobeJ, a tool for high throughput bacterial cell
635 detection and quantitative analysis. *Nat. Microbiol.* **1**, 1–7 (2016).
636 12. Berg, S. *et al.* ilastik: interactive machine learning for (bio)image analysis. *Nat. Methods* **16**,
637 1226–1232 (2019).
638 13. Monahan, L. G., Robinson, A. & Harry, E. J. Lateral FtsZ association and the assembly of the
639 cytokinetic Z ring in bacteria. *Mol. Microbiol.* **74**, 1004–1017 (2009).
640 14. Erickson, H. P., Anderson, D. E. & Osawa, M. FtsZ in Bacterial Cytokinesis: Cytoskeleton and
641 Force Generator All in One. *Microbiol. Mol. Biol. Rev.* **74**, 504–528 (2010).
642 15. Walker, B. E., Männik, J. & Männik, J. Transient Membrane-Linked FtsZ Assemblies Precede Z-
643 Ring Formation in Escherichia coli. *Curr. Biol.* **30**, 499–508.e6 (2020).
644 16. Ellefsen, K. L., Dynes, J. L. & Parker, I. Spinning-Spot Shadowless TIRF Microscopy. *PLOS ONE*
645 **10**, e0136055 (2015).
646 17. Luisier, F., Vonesch, C., Blu, T. & Unser, M. Fast interscale wavelet denoising of Poisson-
647 corrupted images. *Signal Process.* **90**, 415–427 (2010).
648 18. Haydon, D. J. *et al.* An Inhibitor of FtsZ with Potent and Selective Anti-Staphylococcal Activity.
649 *Science* **321**, 1673–1675 (2008).
650 19. McGorty, R., Kamiyama, D. & Huang, B. Active microscope stabilization in three dimensions
651 using image correlation. *Opt. Nanoscopy* **2**, 3 (2013).
652 20. Gamba, P., Veening, J.-W., Saunders, N. J., Hamoen, L. W. & Daniel, R. A. Two-Step Assembly
653 Dynamics of the Bacillus subtilis Divisome. *J. Bacteriol.* **191**, 4186–4194 (2009).
654 21. Westfall, C. S. & Levin, P. A. Bacterial Cell Size: Multifactorial and Multifaceted. *Annu. Rev.*
655 *Microbiol.* **71**, 499–517 (2017).
656 22. Dajkovic, A., Pichoff, S., Lutkenhaus, J. & Wirtz, D. Cross-linking FtsZ polymers into coherent Z
657 rings. *Mol. Microbiol.* **78**, 651–668 (2010).
658 23. Caldas, P. *et al.* Cooperative ordering of treadmilling filaments in cytoskeletal networks of FtsZ
659 and its crosslinker ZapA. *Nat. Commun.* **10**, 5744 (2019).
660 24. Huecas, S. *et al.* Self-Organization of FtsZ Polymers in Solution Reveals Spacer Role of the
661 Disordered C-Terminal Tail. *Biophys. J.* **113**, 1831–1844 (2017).

662 25. Sundararajan, K. & Goley, E. D. The intrinsically disordered C-terminal linker of FtsZ regulates
663 protofilament dynamics and superstructure in vitro. *J. Biol. Chem.* **292**, 20509–20527 (2017).
664 26. Buske, P. J. & Levin, P. A. A flexible C-terminal linker is required for proper FtsZ assembly in
665 vitro and cytokinetic ring formation in vivo. *Mol. Microbiol.* **89**, 249–263 (2013).
666 27. Denk, J., Huber, L., Reithmann, E. & Frey, E. Active Curved Polymers Form Vortex Patterns on
667 Membranes. *Phys. Rev. Lett.* **116**, 178301 (2016).
668 28. Pasquina-Lemonche, L. *et al.* The architecture of the Gram-positive bacterial cell wall. *Nature*
669 **582**, 294–297 (2020).
670 29. Coltharp, C., Buss, J., Plumer, T. M. & Xiao, J. Defining the rate-limiting processes of bacterial
671 cytokinesis. *Proc. Natl. Acad. Sci.* 201514296 (2016) doi:10.1073/pnas.1514296113.
672 30. de Jong, I. G., Beilharz, K., Kuipers, O. P. & Veening, J.-W. Live Cell Imaging of Bacillus subtilis
673 and Streptococcus pneumoniae using Automated Time-lapse Microscopy. *J. Vis. Exp.* (2011)
674 doi:10.3791/3145.
675 31. Harwood, C. R. & Cutting, S. M. *Molecular biological methods for Bacillus*. (Wiley, 1990).
676 32. Koo, B.-M. *et al.* Construction and Analysis of Two Genome-Scale Deletion Libraries for Bacillus
677 subtilis. *Cell Syst.* **4**, 291–305.e7 (2017).
678 33. Ellefsen, K. L., Dynes, J. L. & Parker, I. Spinning-Spot Shadowless TIRF Microscopy. *PLOS ONE*
679 **10**, e0136055 (2015).
680 34. Thevenaz, P., Ruttimann, U. E. & Unser, M. A pyramid approach to subpixel registration based
681 on intensity. *IEEE Trans. Image Process.* **7**, 27–41 (1998).
682 35. Dos Santos Caldas, P. R., Radler, P., Sommer, C. M. & Loose, M. Computational analysis of
683 filament polymerization dynamics in cytoskeletal networks. *Methods Cell Biol.* (2020).
684 36. Eberly, D., Gardner, R., Morse, B., Pizer, S. & Scharlach, C. Ridges for image analysis. *J. Math.*
685 *Imaging Vis.* **4**, 353–373 (1994).
686 37. Tinevez, J.-Y. *et al.* TrackMate: An open and extensible platform for single-particle tracking.
687 *Methods* **115**, 80–90 (2017).
688 38. Ho, J., Tumkaya, T., Aryal, S., Choi, H. & Claridge-Chang, A. Moving beyond P values: data
689 analysis with estimation graphics. *Nat. Methods* **16**, 565–566 (2019).
690